Direct detection system for full-field nanoscale X-ray diffraction-contrast imaging

Elliot Kisiel,[1,2,*] Ishwor Poudyal,[2,3] Peter Kenesei,[2] Mark Engbretson,[2] Arndt Last,[4] Rourav Basak,[1] Ivan Zaluzhnyy,[1] Uday Goteti,[1] Robert Dynes,[1] Antonino Miceli,[2] Alex Frano,[1] and Zahir Islam[2]

[1]*Physics Department, University of California - San Diego, 9500 Gilman Dr., La Jolla, CA 92093, USA*
[2]*X-ray Science Division, Argonne National Laboratory, 9700 S Cass Ave., Lemont, IL 60439, USA*
[3]*Materials Science Division, Argonne National Laboratory, 9700 S Cass Ave., Lemont, IL 60439, USA*
[4]*Karlsruhe Institute of Technology, Institute of Microstructure Technology, Hermann-von-Helmholtz-Platz 1, Eggenstein-Leopoldshafen D-76344, Germany*

[*]*ekisiel@ucsd.edu*

Abstract: Recent developments in X-ray science provide methods to probe deeply embedded mesoscale grain structures and spatially resolve them using dark field X-ray microscopy (DFXM). Extending this technique to investigate weak diffraction signals such as magnetic systems, quantum materials and thin films prove challenging due to available detection methods and incident X-ray flux at the sample. We present a direct detection method developed in conjunction with KAImaging which focuses on DFXM studies in the hard X-ray range of 10s of keV and above capable of approaching nanoscale resolution. Additionally, we compare this direct detection scheme with routinely used scintillator-based optical detection and achieve an order of magnitude improvement in exposure times allowing for imaging of weakly diffracting ordered systems.

1. Introduction

Developments in X-ray optics and synchrotron sources have opened up new investigation pathways into structural microscopy techniques capable of sub-micron resolution. Of particular interest recently is dark-field X-ray microscopy (DFXM) [1] which provides a full-field, non-destructive glimpse into deep embedded grain structures with resolutions on the order of 100 nm. To achieve such a feat, X-ray optics placed in the diffracted beam provide a reciprocal space-sensitive spatial mapping of the diffracting grain (Fig. 1). However, this presents challenges due to the relatively low efficiency of many X-ray optics [2 ,3]. This becomes even more challenging if one needs to study charge and magnetic ordering in quantum materials. The intensity problem becomes even worse in 2D systems, such as thin films of compounds of low-Z elements, where the scattering volume is significantly reduced and atomic scattering factors are weaker. For such systems, higher collection times result in lower resolution due to mechanical instabilities present in instruments, reducing many of the advantages of the technique. Extensions of this technique to low-intensity systems open up a plethora of new investigation pathways.

In most DFXM experiments up to now, large grains in polycrystalline samples have been used for the investigation of their structural properties [4–8]. This technique has been pushed to extend to more exotic cases such as pulsed-laser dynamics, weakly-scattering thin films and non-structural Bragg peaks. Although thin films have been studied since the development of DFXM, most of these samples contained elements with large cross-sections and thicker films (>200 nm) [9,10]. Extending DFXM to films with low-Z elements, and spin-charge ordered compounds is necessary for a wider impact in materials research. Even with state-of-the-art light sources, all these instances typically produce signals that are impractical, often times impossible,

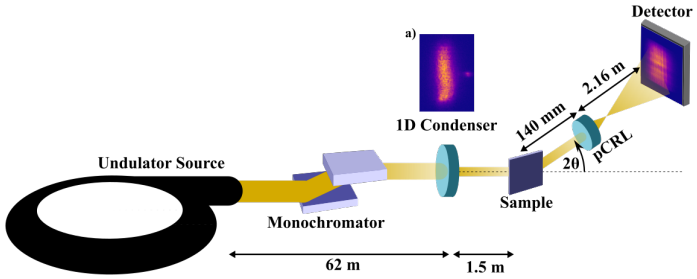

Fig. 1. A diagram depicting the setup of the DFXM scope with a polymeric CRL (pCRL) objective lens placed in the beam path of the diffracted beam. (a) depicts an image of the direct beam with the 1D condenser lens taken in the bright field.

to use for imaging with DFXM. To address this problem, we require either introducing a higher photon flux at the sample, achievable with a condenser lens, or improving the overall measurement efficiency. The first option reduces the illuminated volume of the sample and effectively limits the full-field capabilities of this method. Improving optics efficiencies is difficult due to the limited number of materials that can be used for X-rays optics. This leaves improvements at the detector in the form of direct X-ray detection methods well suitable for DFXM.

Current detection methods for DFXM use indirect detection approaches where X-ray photons are converted to optical photons using a scintillator in combination with a high-resolution optical sensor. A primary advantage of this is an additional magnification arising from a lens placed between the scintillator and the camera. A shortcoming of using this detection method, however, is a reduction by several orders of magnitude in intensity at the optical sensor requiring longer collection times. When using a technique such as DFXM, diffraction signals from the sample are attenuated due to the X-ray objective lens. This can result in limitations of the timescales of dynamics that can be explored as well as compromise observations of weakly diffracting systems. Moreover, these scintillation-based detection systems become increasingly challenging at higher energies, for which thicker scintillation crystals are needed to increase x-ray absorption, resulting in a lower resolution and degradation of signal-to-noise ratio due to increased afterglow effects [11–13]. These complications can be addressed by utilizing a detector meant for the direct detection of hard X-rays at the cost of the additional optical magnification present in the scintillation-based system. One current problem with direct detection X-ray systems is their large pixel size (50 - 200 µm) which is incompatible with full-field, high-resolution, microscopy applications. Development of a novel 8 µm pixel pitch direct detector in conjunction with KA Imaging Inc. (Ontario) provides one solution to the limitations of current detector systems [14]. This detector system was developed to be implemented in High-Energy Diffraction Microscopy, Bragg Coherent Diffraction Imaging (BCDI) and DFXM setups at the Advanced Photon Source (APS). We present the first implementation and characterization of this detector for hard X-ray DFXM.

2. Methods and materials

Full-field dark-field X-ray microscopy (DFXM) operates in a normal diffraction setup with the only exception being the introduction of an X-ray objective lens post-diffraction to spatially resolve the illuminated portion [1,3]. The typical setup for such a technique is shown in Fig. 1 where the lens is placed into the path of the diffracted beam. We leveraged the 6-ID-C station at the APS of Argonne National Laboratory which is equipped with a high-resolution diffractometer. A 1D condenser lens was placed into the path of the incident beam to increase the flux and reduce the footprint on the sample.

The resulting approximate beam size is 70 µm vertically and 10 µm horizontally with a footprint of 70 µm × 65 µm at the Bragg angle of the sample, well matched to the field of view of the objective. For the objective lens, we used a polymeric compound refractive lens (pCRL) optimized for 20 keV [3]. This particular lens focuses in 2D, with a focal length of 131 mm and an effective aperture of 68 µm × 68 µm. The scintillator used is 20 µm thick LuAG:Ce. An optical magnification of a factor of 5 is combined with an optical camera, an Andor Zyla sCMOS camera with a pixel pitch of 6.5 µm. The virtual pixel size of the ID system is therefore 1.3 µm. While the maximum frame rate for the Andor Zyla system is 100 Hz, the low measurement efficiency of the scintillation-based system requires longer exposures dropping the effective frame rate to 1 - 0.1 Hz. We compare this optical setup, hereafter indirect detection (ID), against a 16-megapixel (4096 × 4096) KAImaging BrillianSe amorphous selenium (a-Se) detector, hereafter referred to as direct detection (DD) [14]. A summary features of these detectors is given in Table 1. This detector has a pixel pitch of 8 µm, a nominal thickness of 100 µm, and is capable of capturing X-ray images directly. In addition to this pixel size, the BrillianSe system has other features which make it ideal for use in a DFXM setting.

Table 1. Comparison of the various aspects of the two different detector systems being used in this paper.[a]

Detector	Detection	Max Frame Rate	QE	Pixel Size	Exposure
Andor Zyla (ID)	LuAG:Ce (20 µm)	100 Hz	80 %	1.3 µm	10 s
BrillianSe (DD)	a-Se (100 µm)	2 Hz	90 %	8.0 µm	0.01 s

[a]The Andor Zyla camera is used as the ID scheme while the BrillianSe is used for the DD scheme. The pixel size given for the Andor Zyla detector is the virtual pixel size accounting for the 5× optical magnification. QE is the maximum achievable quantum efficiency at 20 keV for each system's detection. The quoted exposure time is the time necessary to collect images on both detectors with similar signal-to-noise ratios.

One aspect that is of particular interest and a key reason for the development of this system is the extension of this detector to higher energies. For the current setup, we utilize 20 keV X-ray energy which results in a quantum efficiency of roughly 90% making the BrillianSe detector ideal for low-intensity signals coming from weakly-scattering thin film samples. This is in comparison to the Andor Zyla system which has an 80 % quantum efficiency at the wavelength of the LuAG:Ce scintillation wavelength. The Andor Zyla can operate in either a global or rolling shutter architecture, though a rolling shutter architecture is used for comparison in this study. The BrillianSe detector has an operating frame rate of 2 Hz and only operates in a split rolling shutter architecture. This frame rate is limited by the readout times of 1865 ns per pixel with each column of 128x2048 pixels requiring a minimum 489 ms to read leading to a maximum frame rate of 2 Hz. However, our DFXM images typically only occupy 200 × 250 pixels. Future firmware upgrades will enable an increased frame rate for a selected region-of-interest. As this detector also operates in a rolling shutter architecture, each column begins its exposure at its bottom row of pixels and overlaps the next row's exposure with the reading of the current row's exposure. The material a-Se is optimal for use as a photoconductor due to its large bandgap energy (2.3 eV) leading to no free carriers at room temperature, high avalanche gain and low quantum noise when used for high-energy photons. This however requires high voltages to operate (10 kV/mm) and requires that the detector remain below the glass transition temperature of a-Se of 30 °C [15,16]. The resulting system has a low-leakage current (< 1 pA$\cdot$ mm^{-1}), high dynamic range, and high signal-to-noise ratios (SNR) (~ 5) based on prior studies [14]. Further details about the operation and architecture of this system can be found elsewhere [14].

Comparing two different detectors is a challenging prospect due to variations between sensors, materials and other variables. To rectify this, we opted to examine experimental performances using three metrics as our comparison: exposure times, resolution, and feature detection. To

compare the required exposure times between the two different detectors, we settled on exposure times that provided the same signal-to-noise ratio between the peak signal and the background. Comparing the two exposure times in this situation gives a rough estimate of the measurement efficiency between the two detector systems. For the resolution, we used a sample that has periodic spatial modulation with bright and dark fringes neighboring each other to act as a line pair. However, since the sample is positioned in a reflection geometry, our in-plane resolution will be larger due to the compression of reflected regions along a pixel's line of sight. To rectify this and provide a secondary measure in the out-of-plane resolution, we used a weakly damaged sample which also provides a manner for determining detectable features.

The sample we are using as a test is epitaxially grown 40 nm thick $YBa_2Cu_3O_{7-x}$ (YBCO) thin film on an [001] LSAT substrate with a CeO_2 buffer layer roughly 50 nm thick. The LSAT substrate thickness is 500 µm and the sample size is 5×5 mm^2. This sample shows distinct periodic lines (Fig. 2) which can be resolved in both DD and ID allowing for comparison of size and resolution. The spatial period of these lines was determined to be 25 µm with an approximate width of 10 µm. Due to the sensitivity of the DD, comparisons in bright-field mode are not possible which is why this sample was chosen as the distinct vertical lines provide a dark-field comparison of size and resolution. The sample was irradiated with a He^+ beam with a fluence of $2x10^{15}$ ions/cm^2 irradiated at 90 keV to induce defects in the sample. He-ion irradiation is an effective tool for introducing defects in a controlled way. We chose films with certain defects as an example to determine detectable feature sizes suitable to our current setup.

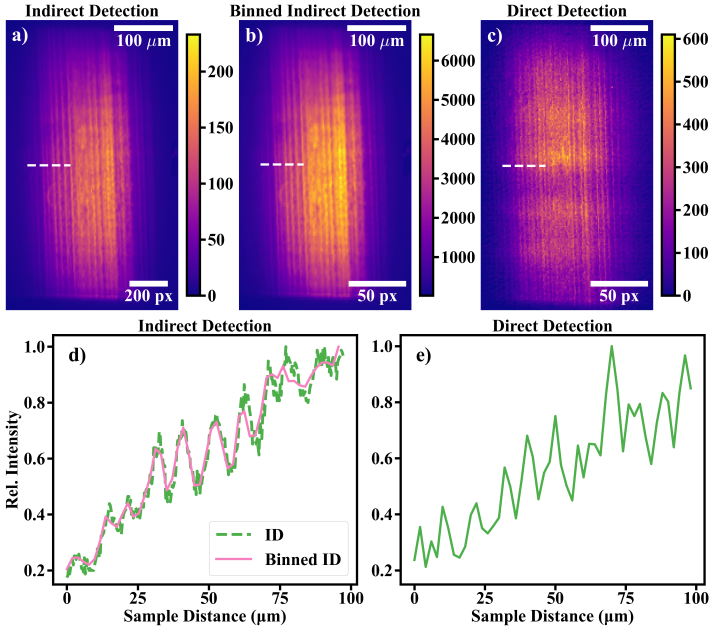

Fig. 2. Examples of the lateral spatial modulation in the sample seen in both indirect detection (ID) images and the direct detection (DD) images. (a) An image taken of the lateral modulations using the ID system. (b) A binned 6×6 image of the ID image for a comparable virtual pixel size with DD. (c) A DD image using the same position and Bragg conditions as ID. (d) Line cuts of the ID and binned ID images along the line indicated in the images. (e) A line cut of the DD image matching the same position as in (d).

3. Results and discussion

To compare these two detection methods, we assess adequate exposure times, resolution, and feature identification and size in dark-field mode. We aligned our diffracted beam on the (006) $YBa_2Cu_3O_7$ (YBCO) Bragg peak and the (002) peak for the $(LaAlO_3)_{0.3}(Sr_2TaAlO_6)_{0.7}$ (LSAT) in the same sample position for a direct comparison of images. Each peak above corresponds to a Bragg angle of 9.12° and 9.41° respectively in reflection geometry. Images of the LSAT substrate were taken at 1 s exposure lengths for the ID image and 10 ms exposures for DD. Images were taken using a 12-bit dynamic range for both detectors and are shown here with a flat-field correction and have their backgrounds subtracted. These times were chosen to match relative grey values in the images with respect to the background to have an appropriate comparison across both detectors.

In terms of exposure time, a normalization across the two detectors using the peak-to-background ratio gives an appropriate metric for comparison. Although we utilized the lowest exposure time for ID images that provided a comparable peak-to-background ratio, the maximum counts above the background for ID were only 200 cps. Higher counts are often necessary to improve analysis and provide better statistics on features. In comparison, for the given times, DD provides a much higher maximum count of 600 cps above background indicating that a further reduction in exposure times is possible. This possibly indicates that the exposure times for the DD system may have been chosen to be too long, though vertical fluctuations become more evident and often obscure portions of the signal. These vertical fluctuations can be seen in the intensity profiles at faster exposure times (< 100 ms) coming from a combination of the rolling shutter architecture and incident intensity variation due to mechanical vibrations from the monochromator cryo pump (Fig. 2(c)).

One consideration for the faster exposure time is the larger effective size of the pixels in the DD system in comparison to ID. As previously mentioned, the virtual pixel size of the scintillator is 1.3 μm while the pixel size of the DD system is 8 μm. The factor of 36 increase in the area of the pixels between the two systems results in more X-ray flux per pixel. However, when binning the ID image into 6×6 summed pixels, we can see from Fig. 2 that the overall intensity increases but some features become less resolved. The resolution also drops to 3-4 pixels in the ID image as compared with the 2 pixels observable in DD image as determined from the line profile analysis demonstrated later. Comparing these binned ID and DD images can also provide a comparison of experimental detector efficiency.

We can give a rough estimate of the experimental efficiency between the ID and DD systems by comparing the images of the binned ID and DD. Comparing similar regions and accounting for two orders-of-magnitude time difference between the two, the binned ID (Fig. 2(b)) has a maximum pixel count of 6000 counts per second whereas the DD system (Fig. 2(c)) has a maximum of 60000 counts per second. This gives a rough estimate of an order-of-magnitude improvement in the experimental efficiency of DD over ID. One additional advantage to these fast collection times is the ability to observe dynamics on the millisecond timescale.

In terms of resolution, we first determine that the magnification arising from the X-ray objective lens is ~ 26× with an additional 5× from optical magnification. The line profile and the corresponding image (Fig. 3) allow us to determine the resolution, giving 1.9 ± 0.1 μm transverse resolution for a line pair. This is determined by the transition between the modulations as illustrated in Fig. 3(b). A logistic function is fit to these line cuts for many line pairs and the full-width-at-half-max (FWHM) of its derivative is reported here (only one line cut is shown here). Although this method only yields an upper bound for the resolution, this still provides a valuable metric for comparison.

Performing a similar process on the DD method (Fig. 4), we obtain the transverse resolution to be 2.2 ± 0.3 μm resolution for a line pair. Due to limiting feature size and the higher acquisition time on the ID method, the resolution is lower than the previously determined experimental

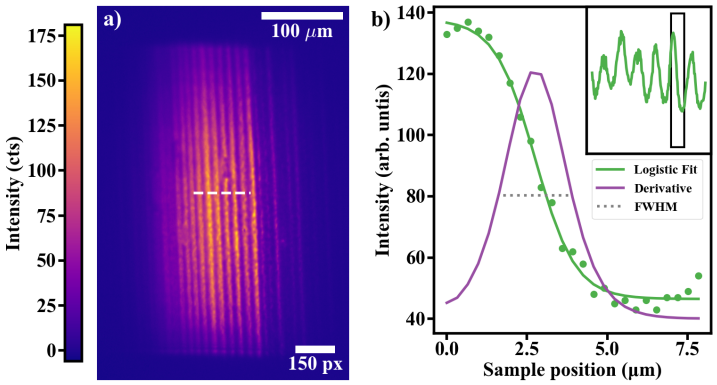

Fig. 3. The ID image (a) with the corresponding line cut (b) to determine the resolution. The inset shows the region from the line cut indicated by the white line in the image. The width is 0.9 μm leading to a resolution on the order of 1.9 ± 0.1 μm. The green line in (b) indicates the fit logistic function while the purple indicates its derivative. The full-width at half-max is indicated by the dotted gray line

resolution of 480 nm [3], determined using a Siemens star in bright-field. As previously noted, the use of the DD in bright-field is not possible and the current sample only provides an upper bound on the resolution due to the feature size.

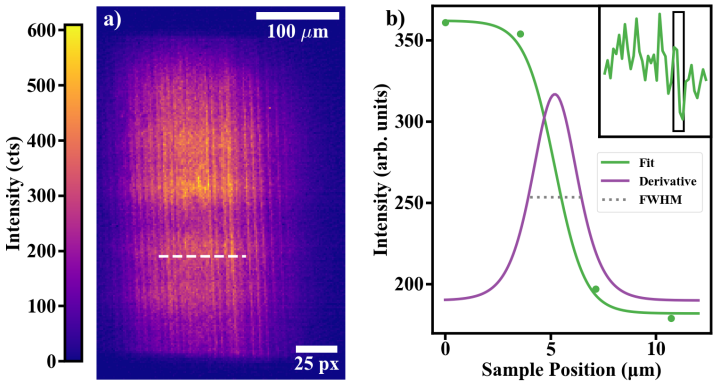

Fig. 4. The DD image (a) with the corresponding line cut (b) to determine the resolution. The inset in (b) indicates the line profile of the white dotted line in the image. The width is 1.1 μm leading to a resolution of 2.2 ± 0.3 μm. This is a comparable resolution to that of the ID due to the limiting feature size and vibrational distortions associated with the longer exposure required in the indirect measurements. The green line in (b) indicates the fit logistic function while the purple indicates its derivative. The full-width at half-max is indicated by the dotted gray line.

For the resolvable features as well as the resolution in the out-of-plane direction, we utilized a weakly damaged sample with varying sizes and random defect locations to study. The size of these defects ranges from 1 μm to 5 μm in extent, providing a good range to determine visibility. A comparison of the YBCO layer defects can be seen in Fig. 5 which has a large gap matching in both the ID and DD images with a size of 11 μm × 17 μm. Relative tilts between detectors due to mechanical mounting schemes and internal optics of the ID system can account for small differences in the lateral positions and orientations of lines between ID and DD systems. While

the larger (>3 μm) features are visible on the DD sensor, smaller features becoming increasingly hard to separate from noise. Additionally, the resolution comparison in the out-of-plane direction is 1.4 ± 0.1 μm for DD and 1.4 ± 0.1 μm ID. Although the resolution for both detectors is comparable, the limitations to the DD system stem from the detectable feature size.

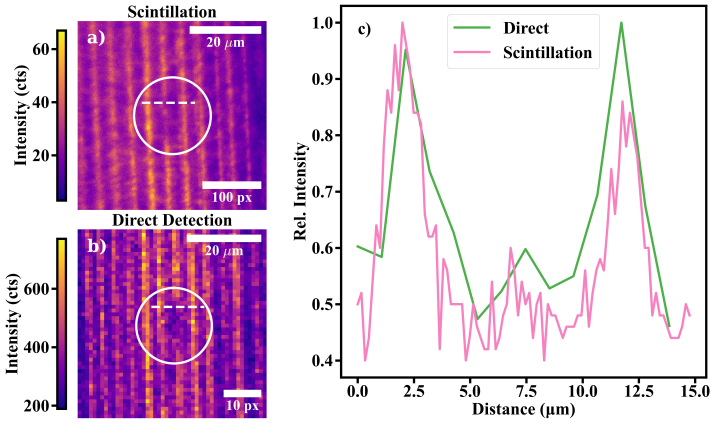

Fig. 5. Image of the YBCO layer showing the same defects in both the ID (a) and DD (b) images. The corresponding line cut profiles are given in (c) for comparison from the dotted lines in (a), (b).

4. Conclusion

We presented a novel high-efficiency direct-detection method for use in DFXM to enable its applicability to systems with weaker diffraction signals such as a small single-crystal grain, charge and magnetic order domains, and thin films with high efficiency and throughput, albeit at the expense of some resolution. Since DD images were collected at exposure times faster than timescales of mechanical instabilities, vibrational correction algorithms were not necessary. Although ID method has a smaller virtual pixel size, a longer exposure time (>100 ms) makes resolution susceptible to ever-present mechanical instabilities. Consequently, unless ID DFXM images with a good signal-to-noise ratio are collected with exposure times of the order of tens of milliseconds vibrational correction algorithms are ineffective. By increasing sample-to-detector distance (e.g., 5 m) and using a shorter focal length lens, resolution with DD can be improved by more than a factor of two, i.e., $<1\mu$m line pair in the present case.

Additionally, proposed upgrades at the APS to improve coherent flux, exposure times needed for comparable investigations is expected to decrease [17]. As a direct consequence of a lower source emittance, condensers (e.g., polymeric lenses) will deliver the entire monochromatic beam to the sample with an expected twofold increase in X-ray flux. With higher flux, millisecond dynamics and weakly-scattering systems, such as charge and magnetic order domains, and weakly-diffracting thin films can be observed using DFXM. Faster collection rates when combined with vibrational corrections and discrete wavelet analysis feature tracking [18] may allow for observation of millisecond dynamics in low-intensity cases with improved resolution.

For energies beyond 30 keV, scintillation efficiency decreases rapidly and results in lower resolution and poorer image quality. This DD system may extend DFXM to higher energies and techniques requiring high resolution and high-energy such as Bragg coherent diffraction imaging [19]. This type of detector allows DFXM to be extended to a plethora of new materials and regimes previously unexplored using a full-field structural microscopy technique. Overall, access to a DD method with small pixel pitch that is optimized for hard X-rays in a DFXM setting opens up opportunities to new science previously inaccessible to ID methods.

Funding. Basic Energy Sciences (DESC0019273); Argonne National Laboratory (DE-AC02-06CH11357); Oak Ridge Institute for Science and Education (DE-SC0014664).

Acknowledgments. This material is based upon work supported by the U.S. Department of Energy, Office of Science, Office of Workforce Development for Teachers and Scientists, Office of Science Graduate Student Research (SCGSR) program. The SCGSR program is administered by the Oak Ridge Institute for Science and Education for the DOE under contract number DE-SC0014664. This research used resources of the Advanced Photon Source, a U.S. Department of Energy (DOE) Office of Science user facility operated for the DOE Office of Science by Argonne National Laboratory under Contract No. DE-AC02-06CH11357. Materials and samples used in this work were supported as part of the "Quantum Materials for Energy Efficient Neuromorphic Computing" (Q-MEEN-C), an Energy Frontier Research Center funded by the U.S. Department of Energy, Office of Science, Basic Energy Sciences under the Award No. DESC0019273. The authors would like to thank the Karlsruhe Nano Micro Facility (KNMF) for the fabrication of the polymer X-ray optics and the invaluable help from KA Imaging Inc. regarding the BrillianSe detector.

Disclosures. The authors declare no conflicts of interest.

Data availability. Data underlying the results presented in this paper are not publicly available at this time but may be obtained from the authors upon reasonable request.

References

1. H. Simons, A. King, W. Ludwig, *et al.*, "Dark-field x-ray microscopy for multiscale structural characterization," Nat. Commun. **6**(1), 6098 (2015).
2. C. Krywka, A. Last, F. Marschall, *et al.*, "Polymer compound refractive lenses for hard x-ray nanofocusing," AIP Conf. Proc. **1764**, 020001 (2016).
3. Z. Qiao, X. Shi, P. Kenesei, *et al.*, "A large field-of-view high-resolution hard x-ray microscope using polymer optics," Rev. Sci. Instrum. **91**(11), 113703 (2020).
4. S. Ahl, H. Simons, C. Detlefs, *et al.*, "Subgrain dynamics during recovery of partly recrystallized aluminum," Acta Mater. **185**, 142–148 (2020).
5. A. Bucsek, H. Seiner, H. Simons, *et al.*, "Sub-surface measurements of the austenite microstructure in response to martensitic phase transformation," Acta Mater. **179**, 273–286 (2019).
6. L. E. Dresselhaus-Marais, G. Winther, M. Howard, *et al.*, "In situ visualization of long-range defect interactions at the edge of melting," Sci. Adv. **7**(29), eabe8311 (2021).
7. J. E. Daniels, M. Majkut, Q. Cao, *et al.*, "Heterogeneous grain-scale response in ferroic polycrystals under electric field," Sci. Rep. **6**(1), 22820 (2016).
8. C. Yildirim, P. Cook, C. Detlefs, *et al.*, "Probing nanoscale structure and strain by dark-field x-ray microscopy," MRS Bull. **45**(4), 277–282 (2020).
9. C. Yildirim, P. Ballet, J.-L. Santailler, *et al.*, "Role of threading dislocations on the growth of hgcdte epilayers investigated using monochromatic x-ray bragg diffraction imaging," J. Synchrotron Radiat. **28**(1), 301–308 (2021).
10. H. Simons, A. C. Jakobsen, S. R. Ahl, *et al.*, "Nondestructive mapping of long-range dislocation strain fields in an epitaxial complex metal oxide," Nano Lett. **19**(3), 1445–1450 (2019).
11. G. F. Knoll, *Radiation Detection and Measurement* 4th ed. (Wiley, 2010).
12. P. Rodnyi, *Physical Processes in Inorganic Scintillators*, Laser & Optical Science & Technology (Taylor & Francis, 1997).
13. J. H. Siewerdsen and D. A. Jaffray, "A ghost story: Spatio-temporal response characteristics of an indirect-detection flat-panel imager," Med. Phys. **26**(8), 1624–1641 (1999).
14. C. C. Scott, M. Farrier, Y. Li, *et al.*, "High-energy micrometre-scale pixel direct conversion X-ray detector," J. Synchrotron Radiat. **28**(4), 1081–1089 (2021).
15. A. Eisenberg, "Glass transition temperatures in amorphous selenium," J. Polym. Sci. B Polym. Lett. **1**(4), 177–179 (1963).
16. H. Huang and S. Abbaszadeh, "Recent developments of amorphous selenium-based x-ray detectors: A review," IEEE Sensors J. **20**(4), 1694–1704 (2020).
17. B. Borland and M. Oshima, "The Upgrade of the Advanced Photon Source," in *9th International Particle Accelerator Conference* (JACoW Publishing, 2018), pp. 2872–2877.
18. O. Abulshohoud, I. Poudyal, J. McChesney, *et al.*, "A general method for multiresolutional analysis of mesoscale features in dark-field x-ray microscopy images," arXiv (2022).
19. N. Bertaux, M. Allain, J. Weizeorick, *et al.*, "Sub-pixel high-resolution imaging of high-energy x-rays inspired by sub-wavelength optical imaging," Opt. Express **29**(22), 35003–35021 (2021).